JOURNAL OF GUIDANCE, CONTROL, AND DYNAMICS
Vol. 32, No. 6, November–December 2009

Active Optics of Large Segmented Mirrors: Dynamics and Control

R. Bastaits,* G. Rodrigues,* B. Mokrani,* and A. Preumont†
Free University of Brussels, B-1050 Brussels, Belgium

DOI: 10.2514/1.44041

This paper examines the active optics of future large segmented telescopes from the point of view of dynamic simulation and control. The first part of the paper is devoted to the modeling of the mirror. The model has a moderated size and separates the quasi-static behavior of the mirror (primary response) from the dynamic response (secondary or residual response). The second part of the paper is devoted to control. The control strategy considers explicitly the primary response of the telescope through a singular value controller. The control-structure interaction is addressed with the general robustness theory of multivariable feedback systems, where the secondary response is considered as uncertainty. This approach is very fast and allows extensive parametric studies. The study is illustrated with an example involving 90 segments, 270 inputs, and 654 outputs.

Introduction

MONOLITHIC mirrors of diameter larger than 8 m are difficult to manufacture [1]. As a result, all future large telescopes will be segmented. Currently, telescopes of 30 m and more are under design [2,3], involving several hundreds of segments. Figure 1 shows the primary mirror (M1) of a European extremely large telescope (E-ELT); it has a diameter of 42 m and consists of 984 aspherical segments; every segment is equipped with three two-stage position actuators, controlling the piston and the two tilts, and six edge sensors measuring the position of the segment with respect to its six neighbors. The motion of the position actuators is transmitted to the segment through a whiffle tree. Overall, there are 2952 position actuators $\mathbf{a}$ and 5604 edge sensors $\mathbf{y}_1$.

Modeling for control and controlling large complex active structures such as telescopes poses several challenges:

1) Finite element techniques classically used in structural modeling tend to use a very large number of degrees of freedom that reflect the complex geometry of the structural components. The size of the control model (used in the control design and to evaluate the control-structure interaction) must be drastically reduced while preserving the main features of the system, statically and dynamically. The control model must give access to all actuator inputs, sensor outputs, and optical performance metrics, and it is essential to preserve the kinematic relationship between the position actuators and the quasi-static position of the segmented mirror (primary response).

2) The control algorithm must be simple enough to be implemented in real time (in spite of the large number of inputs and outputs), provide enough gain in low frequency to achieve performance, and enough roll off outside the bandwidth to reduce spillover. A reliable lower bound for the stability margin should be evaluated from the control model, and, if possible, the critical mode(s) for stability should be identified. The control model should allow extensive parametric studies and sensitivity analysis. These challenges have only been partially covered by the existing literature [4–9].

The objective of this study is threefold:

1) To develop a representative numerical model of the segmented mirror and its supporting truss that can be used for control design and robustness evaluation; this model should have a minimum complexity to allow extensive parametric studies and control-structure interaction. In a later stage, we intend to also use it for wind response calculation and optical performance evaluation.

2) To implement a control strategy based on the primary response of the mirror and two sensor arrays, the edge sensors measuring the relative displacements of adjacent mirrors and the normal to the segments.

3) To examine the interaction between the controller and the structural dynamics with various multivariable robustness tests in the frequency domain, where the secondary response is considered as uncertainty, and evaluate the requirements in terms of frequency and damping for the supporting truss to guarantee the performance, control bandwidth, and an appropriate stability margin for the control system.

The system can be represented schematically as in Fig. 2. The position actuator is represented by a force $\mathbf{F}_a$ acting on a spring k_a that is taken as the stiffness of the whiffle tree; the force is related to the unconstrained displacement by $\mathbf{F}_a = k_a\mathbf{a}$. The position actuators rest on a supporting truss carrying the whole mirror. The disturbances $\mathbf{d}$ applied to the system come from thermal gradients, changing gravity vector with the elevation of the telescope, and wind.

Figure 3 describes the temporal and spatial frequency distribution of the various layers of the control system involved in the wave front correction of a large telescope [10]; the spatial frequency is expressed in terms of Zernike modes. In general, adaptive optics operates on a smaller deformable mirror and the amplitudes are small, typically a few microns. Our discussion is focused on M1; the amplitudes to be corrected by the active optics are typically several hundred microns [11].

Currently the control strategy envisaged by the European Southern Observatory (ESO) for cophasing the segments [6,12] assumes that the supporting truss is rigid and that the natural frequency of the whiffle tree (connecting the actuators to the segments) is well above the bandwidth of the control system (which is realistic). In this case, the behavior of the segmented mirror is assumed quasi-static and the kinematic relationship between the actuator displacements $\mathbf{a}$ and the edge sensors output $\mathbf{y}_1$ is simply

$$\mathbf{y}_1 = \mathbf{J}_e\mathbf{a} \tag{1}$$

where $\mathbf{J}_e$ is the Jacobian of the edge sensors of the segmented mirror. Here we assume that the edge sensors are sensitive to the relative displacements normal to the segments only. The pseudoinverse of the Jacobian $\mathbf{J}_e^+$ is best obtained by singular value decomposition (SVD)

$$\mathbf{J}_e = \mathbf{U}\mathbf{\Sigma}\mathbf{V}^T \tag{2}$$

where the columns of $\mathbf{U}$ are the orthonormalized edge sensor modes, the columns of $\mathbf{V}$ are the orthonormalized actuator modes, and $\mathbf{\Sigma}$ contains the singular values on its diagonal. The control system works according to Fig. 4, called SVD controller [5]. $\mathbf{d}$ is the

Received 26 February 2009; revision received 17 June 2009; accepted for publication 23 June 2009.

*Active Structures Laboratory, C.P. 165-42, 50 Avenue Franklin Delano Roosevelt.

†Active Structures Laboratory, C.P. 165-42, 50 Avenue Franklin Delano Roosevelt; andre.preumont@ulb.ac.be. Associate Fellow AIAA.

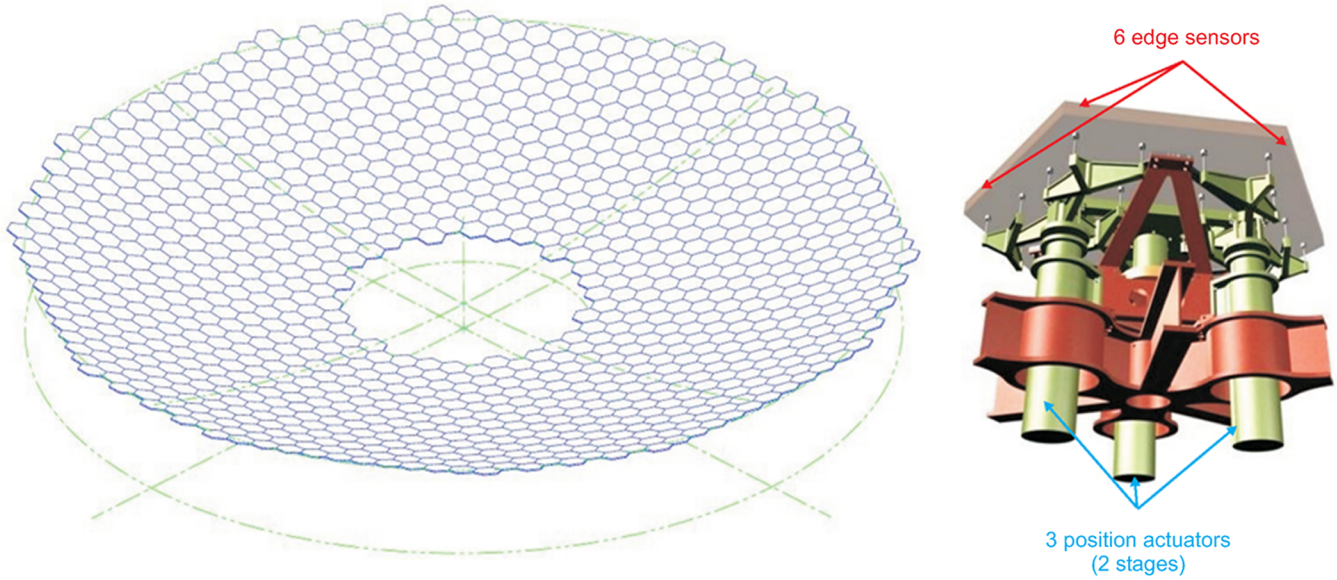

Fig. 1 Primary mirror (M1) of the future E-ELT telescope; it consists of 984 segments, each of them equipped with 6 edge sensors and 3 two-stage position actuators. The segments are connected to the actuators by a whiffle tree (from [6], with permission).

disturbance applied to the mirror, and the set of filters $\mathbf{H}(s)$ provide (it is hoped) adequate disturbance rejection and stability margins (we will come back to this). $H(s)$ may be a scalar function if the same loop shaping is applied to all SVD modes; in this case all the loops have essentially the same control gain. Figure 5 shows a typical distribution of the singular values of $\mathbf{J}_e$ ranked by increasing order; one sees that the lowest singular values are zero (to the numerical accuracy); they correspond to the lowest optical modes, piston, tilt, and defocus, which are unobservable from the particular type of edge sensors used in this study, and the modes with the lowest singular values next to them are astigmatism, trifoil, and coma. In this study we assume that, in addition to the edge sensors, the control system also includes another set of sensors, $\mathbf{y}_2$, measuring the tilt angles of the segments (normal sensor in Fig. 2). Once again, if the supporting truss is rigid there is a linear relationship between the actuator displacements and normal to the segments

$$\mathbf{y}_2 = \mathbf{J}_n \mathbf{a} \tag{3}$$

where $\mathbf{J}_n$ is the Jacobian of the normal to the segments; it is block diagonal, because the two components of the normal to a segment

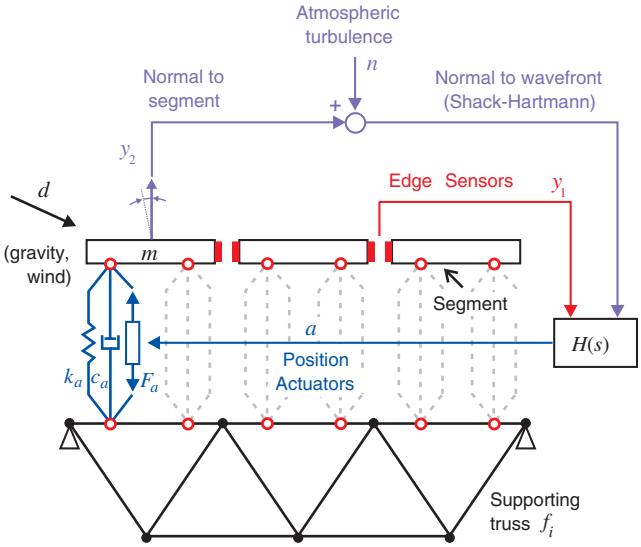

Fig. 2 Active optics control flow for large segmented mirrors; k_a is the stiffness of the whiffle tree and $F_a = k_a a$. The axial DOF at both ends of the actuators are kept in the reduction process.

depend only on the three displacement actuators under that segment. A practical way to measure the normal to the segments is to use a Shack–Hartman sensor (one microlens per segment); however, the Shack–Hartman array measures the normal to the wave front, which, in addition to the normal to the segment, includes the atmospheric turbulence that appears as noise (Fig. 2).[‡]

Structural Dynamics

The dynamics of the mirror consist of global modes involving the supporting truss and the segments and local modes involving the segments alone. The global modes are critical for the control-structure interaction; the segments are designed in such a way that their local modes have frequencies far above the critical frequency range, but their quasi-static response (to the actuator as well as to gravity and wind disturbances) must be dealt with accurately. To handle large optical configurations, it is important to reduce the model as much as possible without losing the features mentioned before. The starting point is a standard finite element (FE) model

$$\begin{pmatrix} \mathbf{M}_{11} & \mathbf{M}_{12} \\ \mathbf{M}_{21} & \mathbf{M}_{22} \end{pmatrix} \begin{pmatrix} \ddot{\mathbf{x}}_1 \\ \ddot{\mathbf{x}}_2 \end{pmatrix} + \begin{pmatrix} \mathbf{K}_{11} & \mathbf{K}_{12} \\ \mathbf{K}_{21} & \mathbf{K}_{22} \end{pmatrix} \begin{pmatrix} \mathbf{x}_1 \\ \mathbf{x}_2 \end{pmatrix} = \begin{pmatrix} \mathbf{f}_1 \\ 0 \end{pmatrix} \tag{4}$$

where the degrees of freedom (DOF) have been partitioned in boundary DOF $\mathbf{x}_1$, including all the loaded ones, especially the axial DOF at both ends of the actuators, at the connection with the truss and the segments (they are highlighted in Fig. 2), and the internal DOF $\mathbf{x}_2$, which are not loaded and may be eliminated by appropriate reduction.

Model Reduction

A Craig–Bampton reduction [13,14] is conducted in two steps. First a Guyan reduction [15] assumes a static relationship between the internal and the boundary DOF

$$\begin{pmatrix} \mathbf{K}_{11} & \mathbf{K}_{12} \\ \mathbf{K}_{21} & \mathbf{K}_{22} \end{pmatrix} \begin{pmatrix} \mathbf{x}_1 \\ \mathbf{x}_2 \end{pmatrix} = \begin{pmatrix} \mathbf{f}_1 \\ 0 \end{pmatrix} \tag{5}$$

leading to $\mathbf{x}_2 = -\mathbf{K}_{22}^{-1}\mathbf{K}_{21}\mathbf{x}_1$. In a second step this solution is enriched by a set of fixed boundary modes, a solution of

$$\mathbf{M}_{22}\ddot{\mathbf{x}}_2 + \mathbf{K}_{22}\mathbf{x}_2 = 0 \tag{6}$$

[‡]Because the bandwidth of the active optics is much lower than the frequency content of the atmospheric turbulence, n can be significantly attenuated by low-pass-filtering.

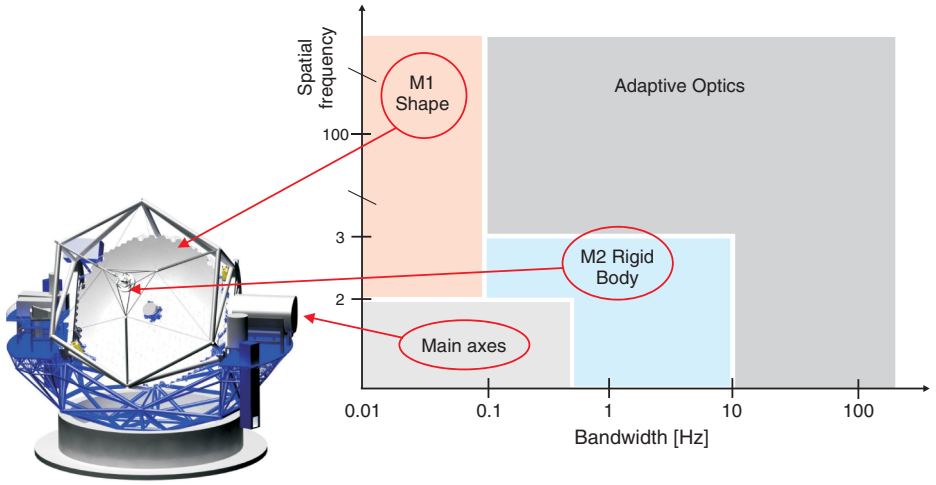

Fig. 3 Temporal and spatial frequency distribution of the various control layers of a large telescope; the spatial frequency is expressed in Zernike modes (adapted from [10]).

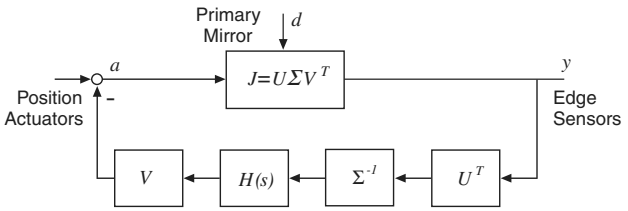

Fig. 4 Block diagram of the cophasing control system (SVD controller) [5].

(obtained by setting $\mathbf{x}_1 = 0$ in [4]); they constitute the column of the matrix $\mathbf{\Psi}_2$ and are normalized according to $\mathbf{\Psi}_2^T \mathbf{M}_{22} \mathbf{\Psi}_2 = 1$. Note that these modes are in a plane orthogonal to the actuators. The number of fixed boundary modes included in the reduction will be discussed shortly. Overall, the coordinate transformation reads

$$\begin{pmatrix} \mathbf{x}_1 \\ \mathbf{x}_2 \end{pmatrix} = \begin{pmatrix} \mathbf{I} & 0 \\ -\mathbf{K}_{22}^{-1}\mathbf{K}_{21} & \mathbf{\Psi}_2 \end{pmatrix} \begin{pmatrix} \mathbf{x}_1 \\ \alpha \end{pmatrix} = \mathbf{T} \begin{pmatrix} \mathbf{x}_1 \\ \alpha \end{pmatrix} \tag{7}$$

where α is the vector of modal amplitude of the fixed boundary modes. Using the transformation matrix $\mathbf{T}$, the mass matrix $\hat{\mathbf{M}}$ and the stiffness matrix $\hat{\mathbf{K}}$ of the reduced system are readily obtained according to the classical formulas

$$\hat{\mathbf{M}} = \mathbf{T}^T \mathbf{M} \mathbf{T} \qquad \hat{\mathbf{K}} = \mathbf{T}^T \mathbf{K} \mathbf{T} \tag{8}$$

leading to the final equation in reduced coordinates

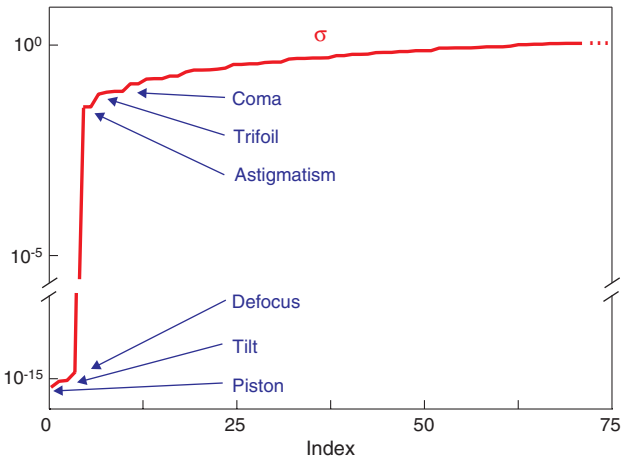

Fig. 5 Singular values of the Jacobian $\mathbf{J}_e$ of the edge sensors, ranked by increasing order. Piston, tilt, and defocus cannot be observed from the edge sensors.

$$\begin{pmatrix} \hat{\mathbf{M}}_{11} & \hat{\mathbf{M}}_{12} \\ \hat{\mathbf{M}}_{12} & \mathbf{I} \end{pmatrix} \begin{pmatrix} \ddot{\mathbf{x}}_1 \\ \ddot{\alpha} \end{pmatrix} + \begin{pmatrix} \hat{\mathbf{K}}_{11} & 0 \\ \mathbf{0} & \mathbf{\Omega}^2 \end{pmatrix} \begin{pmatrix} \mathbf{x}_1 \\ \alpha \end{pmatrix} = \begin{pmatrix} \mathbf{S}_a \mathbf{F}_a + \mathbf{d} \\ \mathbf{0} \end{pmatrix} \tag{9}$$

In this equation the stiffness matrix is block diagonal, with $\hat{\mathbf{K}}_{11} = \mathbf{K}_{11} - \mathbf{K}_{12}\mathbf{K}_{22}^{-1}\mathbf{K}_{21}$ being the Guyan stiffness matrix and $\mathbf{\Omega}^2$ being a diagonal matrix with entries equal to the square of the natural frequencies of the fixed boundary modes. It has been assumed that these are not loaded by the external disturbance $\mathbf{d}$ (wind, gravity, etc.) nor by the control forces $\mathbf{F}_a = k_a \mathbf{a}$. $\mathbf{S}_a$ is the matrix describing the topology of the actuators. To be complete, a damping matrix should be included; this will be done after transformation into modal coordinates. For a segmented mirror with N segments, the size of $\mathbf{x}_1$ is typically $\sim 6N$, down from $> 24N$, depending on the details of the original model shown in Eq. (4). Because of the way they have been selected, the reduced coordinates $\mathbf{x}_1$ describe fully the rigid body motion of the segments and the sensor output can be expressed by

$$\mathbf{y}_1 = \mathbf{S}_{y_1} \mathbf{x}_1 \tag{10}$$

$$\mathbf{y}_2 = \mathbf{S}_{y_2} \mathbf{x}_1 \tag{11}$$

where the matrices $\mathbf{S}_{y_1}$ and $\mathbf{S}_{y_2}$ describe the topology of the sensor arrays.

Modal Analysis

To illustrate our analysis, consider the flat segmented mirror of Fig. 6, consisting of 91 segments supported by a truss. The mass is assumed to be distributed equally between the segments, which are 50 kg each, and the truss, which is 4550 kg. The actuator stiffness k_a has been selected in order that the first piston mode of the segments is 100 Hz. The truss stiffness has been chosen so that the first global mode is $f_1 = 20$ Hz. The modal damping will be assumed uniformly $\xi_i = 0.01$ unless otherwise specified. Figure 7 shows the eigenfrequency distribution of the full FE model; the first 20 or so modes are global modes; their mode shapes are a combination of optical aberration modes of low order. Next follow the local modes of the segments (tilt near 75 Hz and piston near 100 Hz). Figure 8 shows the natural frequencies obtained after the Craig–Bampton reduction described in the previous section, for various numbers of fixed boundary modes. They are solution of [9] after setting the right hand side to zero. One sees that a small number of fixed boundary modes (three in this case) improves the agreement of the eigenfrequency distribution. The mode shapes are displayed in Fig. 9; the frequencies listed at the top of the figure are the natural frequencies of the model; those on the left side are the frequencies of the fixed boundary modes; their relationship with the frequencies of the missing modes in the reduced model is interesting.

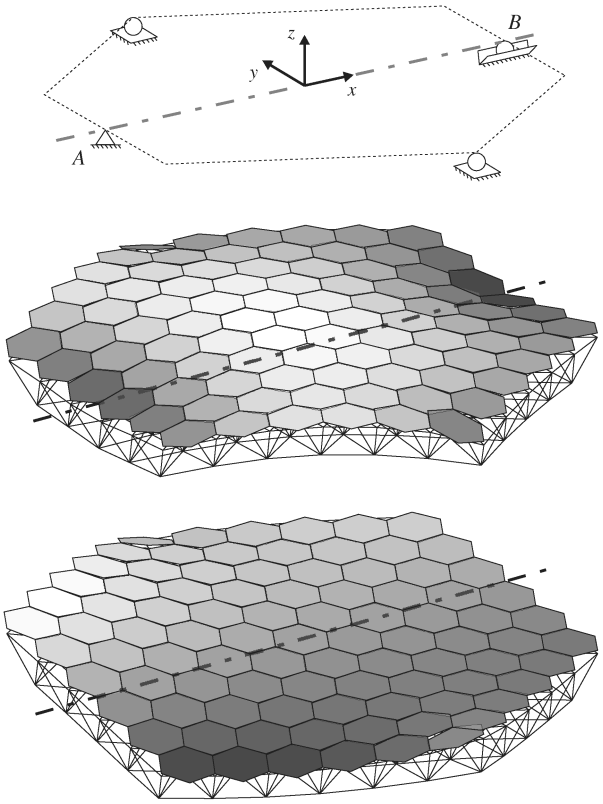

Fig. 6 Segmented mirror consisting of 91 segments supported by a truss. The figure shows the support conditions assumed in this studyand the first modes.

For a large segmented mirror, the model obtained after the Craig–Bampton reduction may be still quite big ($\sim 6N$, down from $>24N$, where N is the number of segments) for coupling it directly with the control; before going into state-space coordinates, it can be further reduced by transforming into modal coordinates and truncating the high-frequency modes that are of no concern in the control-structure interaction analysis. However, the modal truncation must be performed in such a way that the primary response of the structure (i.e., the kinematic relationship between the position actuators and the rigid body motion of the segments) is preserved, as we now examine.

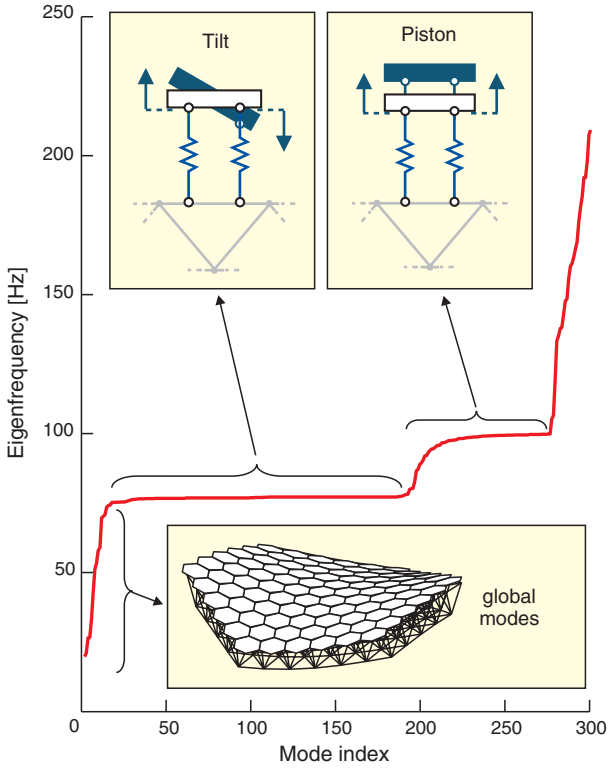

Fig. 7 Eigenfrequency distribution of the full FE model.

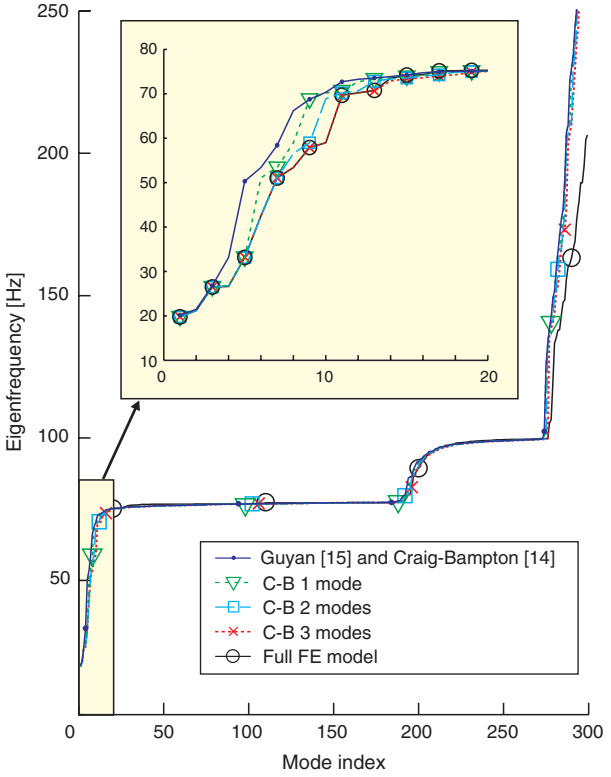

Fig. 8 Eigenfrequency distribution of reduced models (Guyan and Craig–Bampton) easing number of fixed boundary modes.

Static Response

From Eq. (9), the static response of the system is

$$\mathbf{x}_1 = \hat{\mathbf{K}}_{11}^{-1}[\mathbf{S}_a\mathbf{F}_a + \mathbf{d}] \tag{12}$$

$$\mathbf{y}_1 = \mathbf{S}_{y_1}\hat{\mathbf{K}}_{11}^{-1}[\mathbf{S}_a\mathbf{F}_a + \mathbf{d}] = \mathbf{S}_{y_1}\hat{\mathbf{K}}_{11}^{-1}\mathbf{S}_a k_a\mathbf{a} + \mathbf{S}_{y_1}\hat{\mathbf{K}}_{11}^{-1}\mathbf{d} \tag{13}$$

Comparing this equation with Eq. (1), one gets

$$\mathbf{J}_e = \mathbf{S}_{y_1}\hat{\mathbf{K}}_{11}^{-1}\mathbf{S}_a k_a \tag{14}$$

Similarly, using the second output equation, one gets

$$\mathbf{y}_2 = \mathbf{S}_{y_2}\hat{\mathbf{K}}_{11}^{-1}[\mathbf{S}_a\mathbf{F}_a + \mathbf{d}] = \mathbf{S}_{y_2}\hat{\mathbf{K}}_{11}^{-1}\mathbf{S}_a k_a\mathbf{a} + \mathbf{S}_{y_2}\hat{\mathbf{K}}_{11}^{-1}\mathbf{d} \tag{15}$$

and

$$\mathbf{J}_n = \mathbf{S}_{y_2}\hat{\mathbf{K}}_{11}^{-1}\mathbf{S}_a k_a \tag{16}$$

Both $\mathbf{J}_e$ and $\mathbf{J}_n$ can be obtained geometrically without resorting to the FE model.

Dynamic Response

Assume that the eigenvalue problem has been solved for the reduced system and that the eigenmodes have frequencies ω_i and have been normalized to a unit modal mass. Let ϕ_i be the partition of the eigenmodes corresponding to the boundary DOF $\mathbf{x}_1$. Because the control force and the disturbance is only applied to those DOF, the equation governing the dynamic response of mode i is

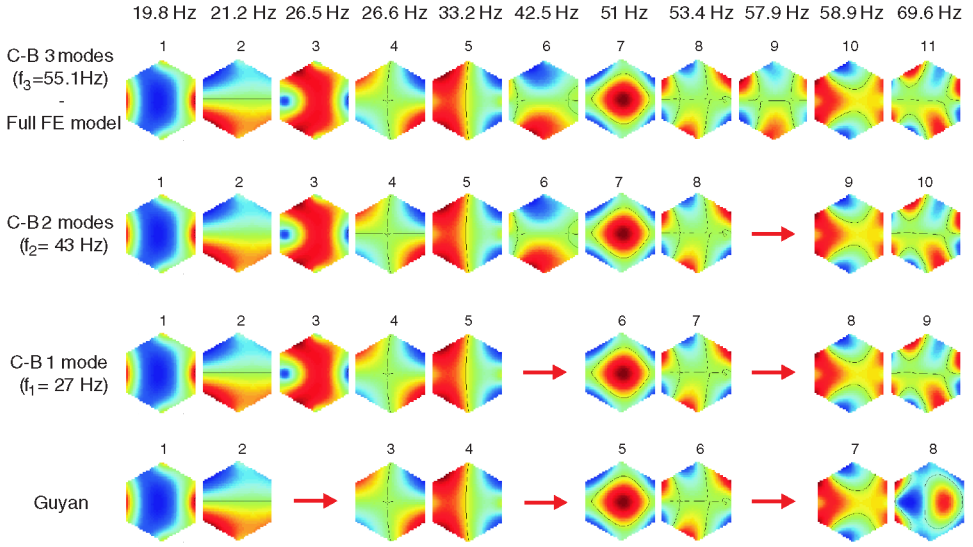

Fig. 9 Eigenmodes of the full model and various reduced models (Craig–Bampton) with an increasing number of fixed boundary modes.

$$\ddot{z}_i + 2\xi_i\omega_i\dot{z}_i + \omega_i^2 z_i = \phi_i^T \mathbf{S}_a \mathbf{F}_a + \phi_i^T \mathbf{d} \qquad (i = 1, \ldots, m) \quad (17)$$

However, only the m lowest frequency modes within or close to the bandwidth of the disturbance respond dynamically; the higher ones ($i > m$) respond in a quasi-static manner and may be regarded as a singular perturbation. The static response of the previous section includes all modes, and if a flexible mode is accounted for dynamically one must remove its contribution to the flexibility matrix. This is obtained by subtracting from $\hat{\mathbf{K}}_{11}^{-1}$ the contribution $\mathbf{F}_m$ of the m modes that respond dynamically according to [16]:

$$\mathbf{F}_m = \sum_{i=1}^{m} \frac{\phi_i \phi_i^T}{\omega_i^2} \quad (18)$$

Thus, the flexibility matrix of the high frequency modes is $\hat{\mathbf{K}}_{11}^{-1} - \mathbf{F}_m$ (depending on m) and the overall dynamic response at the DOF $\mathbf{x}_1$ reads

$$\mathbf{x}_1 = \mathbf{\Phi}_m \mathbf{z} + [\hat{\mathbf{K}}_{11}^{-1} - \mathbf{F}_m][\mathbf{S}_a \mathbf{F}_a + \mathbf{d}] \quad (19)$$

where the components of $\mathbf{z}$ are solutions of Eq. (17) (dynamic response), $\mathbf{\Phi}_m = (\phi_1, \ldots, \phi_m)$ is the matrix of mode shapes at the boundary DOF, and the second term is the quasi-static response (singular perturbation) of all modes beyond m. From Eq. (10), the edge sensor output $\mathbf{y}_1$ is

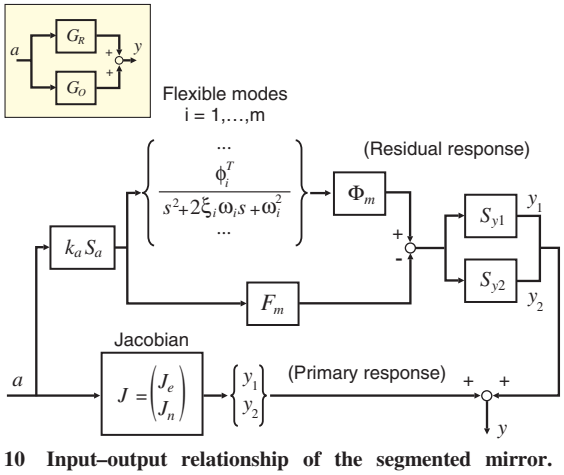

Fig. 10 Input–output relationship of the segmented mirror. The nominal plant $\mathbf{G_0}(s) = \mathbf{J}$ accounts for the primary response and the residual (secondary) response $\mathbf{G}_R(s)$ is regarded as an additive uncertainty.

$$\mathbf{y}_1 = \mathbf{S}_{y_1}\mathbf{x}_1 = \mathbf{S}_{y_1}\mathbf{\Phi}_m\mathbf{z} + [\mathbf{J}_e - \mathbf{S}_{y_1}\mathbf{F}_m\mathbf{S}_a k_a]\mathbf{a} + \mathbf{S}_{y_1}[\hat{\mathbf{K}}_{11}^{-1} - \mathbf{F}_m]\mathbf{d} \quad (20)$$

where Eq. (14) has been used. Similarly, from Eq. (11), the normal sensor output $\mathbf{y}_2$ reads

$$\mathbf{y}_2 = \mathbf{S}_{y_2}\mathbf{x}_1 = \mathbf{S}_{y_2}\mathbf{\Phi}_m\mathbf{z} + [\mathbf{J}_n - \mathbf{S}_{y_2}\mathbf{F}_m\mathbf{S}_a k_a]\mathbf{a} + \mathbf{S}_{y_2}[\hat{\mathbf{K}}_{11}^{-1} - \mathbf{F}_m]\mathbf{d} \quad (21)$$

after using Eq. (15). In these equations, $\mathbf{S}_{y_1}\mathbf{\Phi}_m$ and $\mathbf{S}_{y_2}\mathbf{\Phi}_m$ are the modal components for the first m modes of the edge sensor output and the normal sensor output, respectively. Equations (20) and (21) are reduced to Eqs. (13) and (15) if none of the modes respond dynamically ($m = 0$).

Figure 10 shows a decomposition of the input–output relationship between the primary response $\mathbf{G}_0(s) = \mathbf{J}$ and the residual response $\mathbf{G}_R(s)$; the latter is not taken into account in the controller structure and is regarded as an additive uncertainty.

Control Strategy

Given the size and complexity of the system, its variability with temperature and the elevation angle of the telescope, and the large amount of real-time calculations, it seems reasonable to base the control on the quasi-static behavior of the system and address the dynamic amplification as a perturbation to the nominal system. The baseline cophasing strategy currently envisaged by ESO is the SVD controller of Fig. 4. The edge sensor output $\mathbf{y}_1$ is projected into the sensor modes, $\mathbf{U}^T\mathbf{y}_1$, then scaled according to the inverse of the singular values σ_i^{-1}, shaped in the frequency domain according to the diagonal controller $\mathbf{H}_1(s)$ (possibly variable with the order of the mode), and then applied to the actuator modes through the matrix $\mathbf{V}$

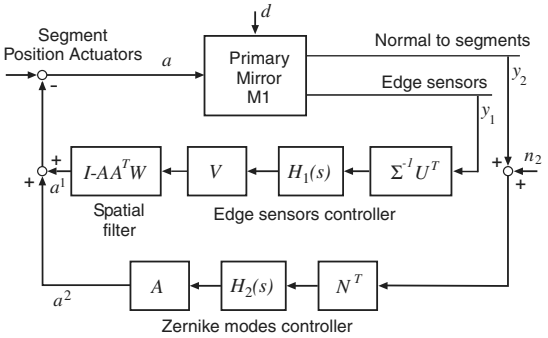

Fig. 11 Block diagram of the dual-loop control strategy for the active optics of M1.

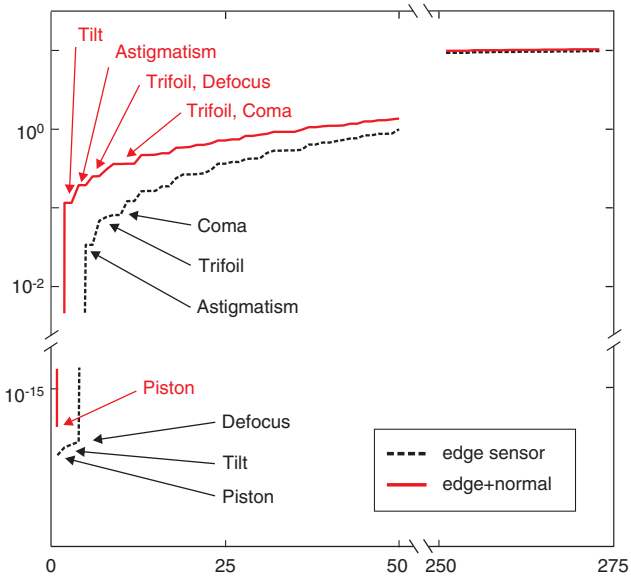

Fig. 12 Comparison of the singular values of the Jacobian $\mathbf{J}_e$ of the edge sensors with the extended Jacobian J (edge sensor measurements and displacement actuators are in meters, tilt angles are in radians).

$$\mathbf{a}^1 = \mathbf{V}\mathbf{H}_1(s)\mathbf{\Sigma}^{-1}\mathbf{U}^T\mathbf{y}_1 \tag{22}$$

This approach reflects the fact that for each mode, the loop gain must be adjusted according to the singular value. If the same scalar controller is used for all loops, they will have the same gain. However, the sensor noise will be amplified on those modes with the lowest singular values (which are the lowest optical modes, Fig. 5). Although [5] concludes that the wave front information is not useful for realistic edge sensor noise, this study assumes a second set of sensors measuring the normal to the segments (tilt), $\mathbf{y}_2$; two controller structures blending this information with the edge sensor output are examined in the next section.

Dual-Loop Controller

The idea consists of using the SVD controller based on the edge sensors for all the modes of the Jacobian $\mathbf{J}_e$ with significant singular values, and to add a second loop based on the normal sensors $\mathbf{y}_2$ to control a selected set of low-order Zernike modes. This is done as follows: let $\mathbf{A} = (\mathbf{a}_1, \ldots, \mathbf{a}_i, \ldots)$ be the matrix, the columns of which

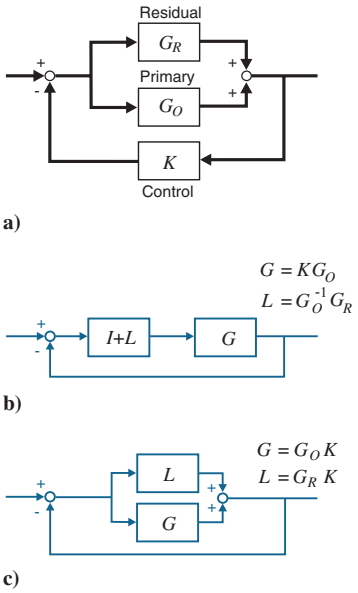

Fig. 13 Block diagram of the control system: a) mirror represented by its primary and residual dynamics, b) multiplicative uncertainty, and c) additive uncertainty.

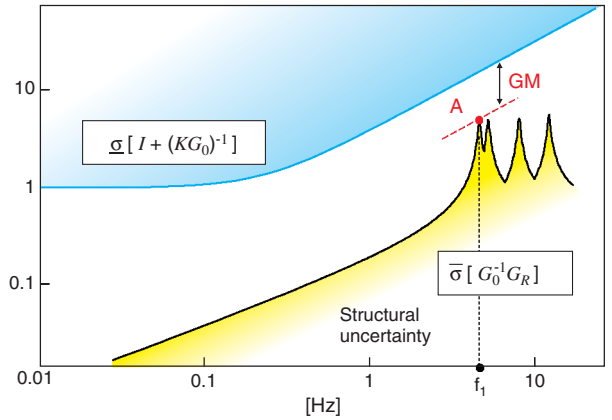

Fig. 14 Robustness test Eq. (30). The minimum singular value $\underline{\sigma}[I + (KG_0)^{-1}]$ refers to the nominal system used in the controller design. The maximum singular value $\bar{\sigma}[G_0^{-1}G_R]$ is an upper bound to the relative magnitude of the residual dynamics. The critical point A corresponds to the closest distance between these curves. The vertical distance between A and the upper curve has the meaning of a gain margin.

are the actuator displacements for the Zernike modes of increasing order. They are assumed to be normalized according to

$$\mathbf{A}^T\mathbf{W}\mathbf{A} = \mathbf{I} \tag{23}$$

(the matrix $\mathbf{W}$ depends on the geometry of the actuator network). Let $\mathbf{N} = (\mathbf{n}_1, \ldots, \mathbf{n}_i, \ldots)$ be the output of normal sensors for the same low-order Zernike modes (with the same normalization). The control input is constructed as follows: the sensor output $\mathbf{y}_2$ is first projected in the space of the selected Zernike modes, $\mathbf{N}^T\mathbf{y}_2$; next, the proper frequency shaping with the diagonal controller $\mathbf{H}_2(s)$ is applied (possibly variable with the order of the mode), and the correction amplitude of the various Zernike modes is then applied to the segment actuators

$$\mathbf{a}^2 = \mathbf{A}\mathbf{H}_2(s)\mathbf{N}^T\mathbf{y}_2 \tag{24}$$

This part of the control includes all the important optical modes of the system. The problem with this dual-loop approach is that the two sets of modes (singular value decomposition of the Jacobian of the edge sensors on the one hand, and Zernike modes on the other) are not orthogonal and that the control input $\mathbf{a}^1$ based on the edge sensors may excite the low-order Zernike modes and vice versa. In fact, the control input $\mathbf{a}^1$ can be made orthogonal to the Zernike modes by passing it through a spatial filter[§]

$$\mathbf{I} - \mathbf{A}\mathbf{A}^T\mathbf{W} \tag{25}$$

Finally,

$$\mathbf{a}^1 = [\mathbf{I} - \mathbf{A}\mathbf{A}^T\mathbf{W}]\mathbf{V}\mathbf{H}_1(s)\mathbf{\Sigma}^{-1}\mathbf{U}^T\mathbf{y}_1 \tag{26}$$

and the control input is $\mathbf{a} = \mathbf{a}^1 + \mathbf{a}^2$. Generated in this way, the control input of the cophasing controller will not excite the optical modes controlled by the dual controller. The cophasing loop, however, may be excited by control input $\mathbf{a}^2$, although weakly, if only those optical modes corresponding to the lowest singular values in $\mathbf{J}_e$ are controlled. Figure 11 shows the block diagram of the dual-loop control strategy previously described.

Note that the piston mode of the mirror is not observable, neither by the edge sensors nor by the normal sensors. In practice, however, the central mirror is removed and its position can be considered as fixed (the edge sensors in the center are attached to the supporting truss).

[§]It is easy to see that this filter will remove any component of the control that belongs to the column space of $\mathbf{A}$ because $(\mathbf{I} - \mathbf{A}\mathbf{A}^T\mathbf{W})\mathbf{A} = 0$ whereas any vector orthogonal to $\mathbf{A}$ will be unaltered, because if $\mathbf{A}^T\mathbf{W}\mathbf{B} = 0$ $(\mathbf{I} - \mathbf{A}\mathbf{A}^T\mathbf{W})\mathbf{B} = \mathbf{B}$.

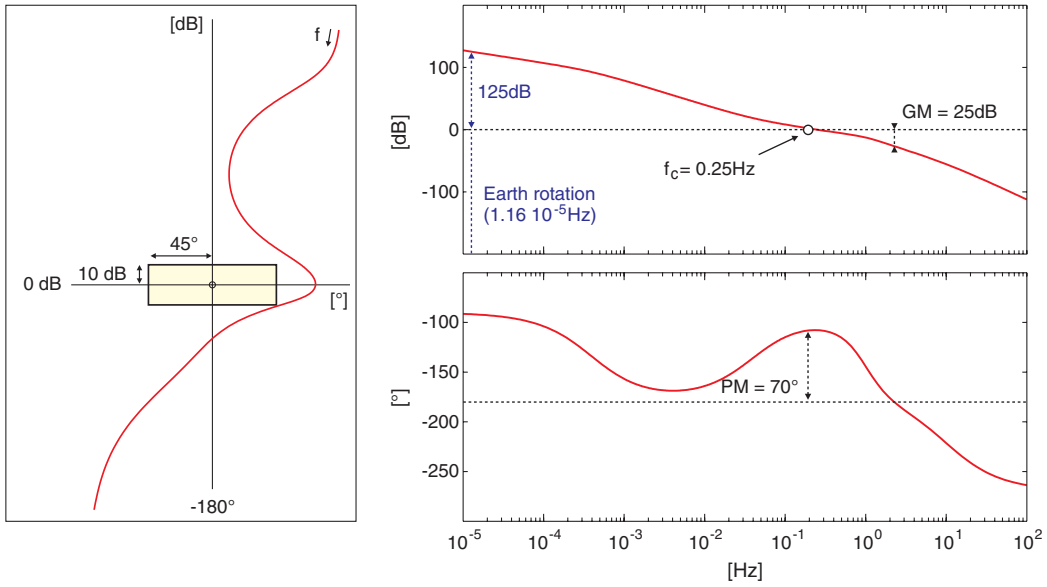

a) b)

Fig. 15 Compensator $h(s)$ common to all loops of the SVD controller. The left-hand side is the Nichols chart [the exclusion zone around the critical point (−180°, 0 dB) corresponds to ($PM = \pm 45°$, $GM = \pm 10$ dB)]. The right-hand side are Bode plots showing the gain of 125 dB at the Earth rotation frequency and a cutoff frequency of $f_c = 0.25$ Hz.

Extended Jacobian Singular Value Decomposition Controller

An alternative way to solve the problem of the poorly observable modes associated with the Jacobian $\mathbf{J}_e$ of the edge sensor consists of building an extended Jacobian coupling the two sets of sensors

$$\mathbf{y} = \begin{pmatrix} \mathbf{y}_1 \\ \mathbf{y}_2 \end{pmatrix} = \begin{pmatrix} \mathbf{J}_e \\ \mathbf{J}_n \end{pmatrix} \mathbf{a} = \mathbf{J}\mathbf{a} \tag{27}$$

The singular values of the Jacobian of the edge sensor $\mathbf{J}_e$ and the extended Jacobian $\mathbf{J}$ are compared in Fig. 12. One sees that except for the global piston mode, which is not observable, the singular values of the extended Jacobian are quite well-conditioned and ready for the implementation of Fig. 4. After conducting an SVD of the extended Jacobian $\mathbf{J} = \mathbf{U}\boldsymbol{\Sigma}\mathbf{V}^T$, the controller reads

$$\mathbf{a} = \mathbf{V}\mathbf{H}(s)\boldsymbol{\Sigma}^{-1}\mathbf{U}^T\mathbf{y} = \mathbf{K}(s)\mathbf{y} \tag{28}$$

with as many modes as necessary. This control strategy is followed in the sequel of this paper.

Control-Structure Interaction

One can see from Fig. 4 that if the mirror would respond in a quasi-static manner, the controller transfer matrix would essentially invert that of the mirror. However, because the response of the mirror includes a dynamic contribution at the frequency of the lowest structural modes and above, the system behaves according to Fig. 10 and the robustness with respect to control-structure interaction must be examined with care [16,17]. The structure of the control system is that of Fig. 13a, where the primary response $\mathbf{G}_0(s)$ corresponds to the quasi-static response described earlier and the residual response $\mathbf{G}_R(s)$ is the deviation resulting from the dynamic amplification of the flexible modes; $\mathbf{K}(s)$ is the controller.

The control-structure interaction may be addressed with the general robustness theory of multivariable feedback systems [18–20], with the residual response being considered as uncertainty. For a multiplicative uncertainty, the standard structure of Fig. 13b applies with $\mathbf{G}(s) = \mathbf{K}(s)\mathbf{G}_0(s)$ and $\mathbf{L} = \mathbf{G}_0^{-1}\mathbf{G}_R$.[¶] A sufficient condition for stability is that

$$\bar{\sigma}[\mathbf{L}(j\omega)] < \underline{\sigma}[I + \mathbf{G}^{-1}(j\omega)], \qquad \omega > 0 \tag{29}$$

[¶]The inverse of rectangular matrices should be understood in the sense of pseudoinverse.

($\bar{\sigma}$ and $\underline{\sigma}$ stand, respectively, for the maximum and the minimum singular value), which is transformed here into

$$\bar{\sigma}[\mathbf{G}_0^{-1}\mathbf{G}_R(j\omega)] < \underline{\sigma}[I + (\mathbf{K}\mathbf{G}_0)^{-1}(j\omega)], \qquad \omega > 0 \tag{30}$$

This test is quite meaningful and is illustrated in Fig. 14. The left-hand side is independent of the controller; it starts from zero at low frequency where the residual dynamics is negligible and increases gradually when the frequency approaches the flexible modes of the mirror structure, which are not included in the nominal model $\mathbf{G}_0$; the amplitude is maximum at the resonance frequencies where it is only limited by the structural damping. The right-hand side starts from unity at low frequency where $|\mathbf{K}\mathbf{G}_0| \gg 1$ ($\mathbf{K}\mathbf{G}_0$ controls the performance of the control system) and grows larger than one outside the bandwidth of the control system where the system rolls off ($|\mathbf{K}\mathbf{G}_0| \ll 1$). The robustness test looks like Fig. 14; the critical point A corresponds to the closest distance between these curves. The vertical distance between A and the upper curve has the meaning of a gain margin GM. When the natural frequency of the structure changes from f_1 to f_1^*, point A moves horizontally according to the ratio f_1^*/f_1 (increasing the frequency will move A to the right). Similarly, changing the damping ratio from ξ_1 to ξ_1^* will change the amplitude according to ξ_1/ξ_1^* (increasing the damping will decrease the amplitude of A).

Alternatively, for an additive uncertainty the standard structure of Fig. 13c applies with $\mathbf{G} = \mathbf{G}_0\mathbf{K}$ and $\mathbf{L} = \mathbf{G}_R\mathbf{K}$; a sufficient condition for stability is

$$\bar{\sigma}[\mathbf{L}(j\omega)] < \underline{\sigma}[I + \mathbf{G}(j\omega)], \qquad \omega > 0 \tag{31}$$

which is translated into

$$\bar{\sigma}[\mathbf{G}_R\mathbf{K}(j\omega)] < \underline{\sigma}[I + \mathbf{G}_0\mathbf{K}(j\omega)], \qquad \omega > 0 \tag{32}$$

Again, the smallest distance between these two curves has the meaning of a gain margin. The stability conditions Eqs. (30) and (32) come from the small gain theorem; being sufficient conditions, they are both conservative and one may be more conservative than the other. In the example considered in the following section, Eq. (30) turns out to be less conservative than Eq. (32) and will be presented alone. Before this, let us consider the frequency shaping of the SVD controller for the nominal (primary) system.

Loop Shaping of the Singular Value Decomposition Controller

The SVD controller is based on the extended Jacobian, with the same compensator applied to all loops, $\mathbf{H}(s) = \mathbf{I}h(s)$ in Eq. (28). Because of the SVD controller structure,

$$\mathbf{KG}_0 = \mathbf{I}h(s) \tag{33}$$

and all the singular values of $\mathbf{KG}_0$ are identical,

$$\sigma[\mathbf{KG}_0] = |h(j\omega)| \tag{34}$$

Similarly, the sensitivity matrix has also identical singular values,

$$\sigma[(\mathbf{I} + \mathbf{KG}_0)^{-1}] = \frac{1}{|1 + h(j\omega)|} \tag{35}$$

and the controller design can be done as a single input/single output controller according to classical techniques [21] or frequency shaping using the Bode integrals [22]. The active optics controller is mostly targeted by low-frequency disturbances associated with the change of the gravity vector with the earth rotation and transient thermal effects, so the controller aims essentially at providing integral control, large gain at the earth rotation frequency, and enough roll-off at high frequency to accommodate for the flexible modes. The behavior near crossover is dictated by stability margins. Figure 15 shows the Bode plots and the Nichols chart of the controller used in this study; the compensator $h(s)$ consists of an integrator, a lag filter, followed by a lead and a second-order Butterworth filter. The crossover is $f_c = 0.25$ Hz and the attenuation at the Earth rotation frequency is 125 dB. The stability margins are clearly visible on the Nichols chart [the exclusion zone around the critical point (−180 deg, 0 dB) corresponds to (PM= ±45°, $GM = \pm 10$ dB)].

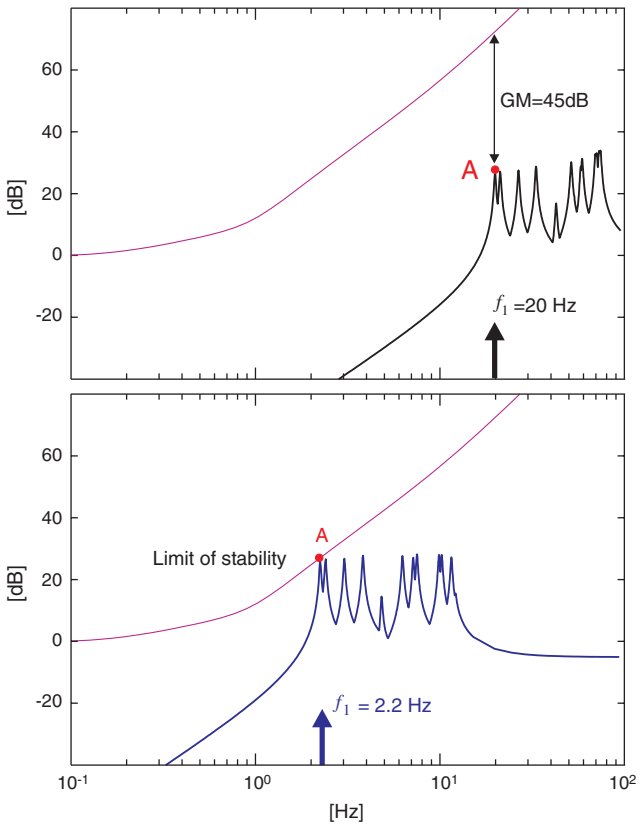

Fig. 16 Robustness test Eq. (30): a) stiff supporting truss ($f_1 = 20$ Hz); the gain margin is $GM = 45$ dB, and b) soft supporting truss at the stability limit.

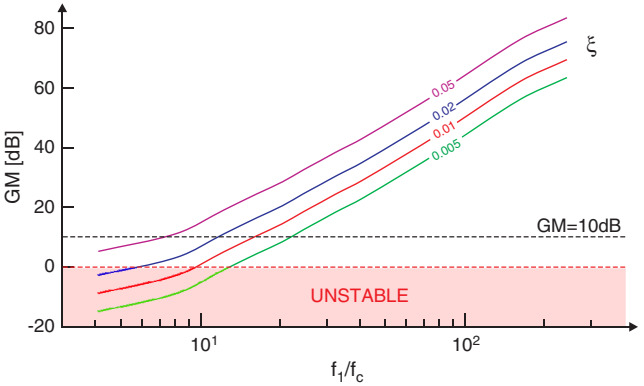

Fig. 17 Evolution of the gain margin with the frequency ratio f_1/f_c for various values of the damping ratio ξ_i.

Discussion

To illustrate the foregoing discussion, consider again the segmented mirror of Fig. 6. Although this example does not correspond to a particular existing telescope, it is representative of the current generation of large telescopes (Keck); the parameters have been chosen so that $f_1 = 20$ Hz and $\xi_i = 0.01$ uniformly. The SVD controller has just been discussed. Figure 16a shows the robustness test Eq. (30); with a ratio $f_1/f_c \simeq 80$ the system exhibits a substantial gain margin of 45 dB with respect to control-structure interaction. To examine more critical configurations that are more representative of extremely large telescopes, the supporting truss is gradually softened by reducing the Young's modulus of the bars forming the truss. Figure 16b shows the stability limit when A touches the upper curve, $f_1 = 2.2$ Hz in this case.** Figure 17 shows the evolution of the gain margin with the frequency ratio f_1/f_c for various values of the damping ratio ξ. According to this plot, if the first structural mode of the supporting structure has a damping ratio of 1%, a gain margin $GM = 10$ requires a frequency separation f_1/f_c significantly larger than 1 decade. This condition may be more and more difficult to fulfill as the size of the telescope grows [23].

Conclusions

This paper has been focused on the control-structure interaction in active optics of large segmented mirrors. In the first part, the numerical modeling of the mirror and its supporting truss structure has been discussed. The primary response (quasi-static) and the residual response (dynamic amplification) have been separated. The control strategy considers explicitly the primary response of the telescope through a singular value controller; the frequency shaping of the loop gain provides the same gain for all loops, large gains at low frequency for performance, roll off at high frequency to limit spillover, and good stability margins near crossover. The control-structure interaction has been addressed with the general robustness theory of multivariable feedback systems where the residual response is considered as uncertainty. This approach is very fast and allows extensive parametric studies. The study has been illustrated with an example involving 90 segments, 270 inputs, and 654 outputs.

References

[1] Bely, P. Y. (ed.), *The Design and Construction of Large Optical Telescopes*, Springer–Verlag, New York, 2003, pp. 151.

[2] Gilmozzi, R., and Spyromilio, J., "The 42 m European ELT: Status," *Ground-Based and Airborne Telescopes II*, edited by L. Stepp, Vol. 7012, Society of Photo-Optical Instrumentation Engineers, Bellingham, WA, 2008, pp. 701219–701219-10.

[3] Nelson, J., and Sanders, G., "The Status of the Thirty Meter Telescope Project," *Ground-Based and Airborne Telescopes II*, edited by L. Stepp, Vol. 7012, Society of Photo-Optical Instrumentation Engineers, Bellingham, WA, 2008, pp. 70121A–70121A-18.

**Note that the robustness test is only a sufficient condition; its failures implies only that instability is possible.

[4] Angeli, G. Z., Upton, R., Serguson, A., and Ellerbroek, B., "Active Optics Challenges of a Thirty meter segmented mirror telescope, Second Backaskog Workshop on Extremely Large Telescopes," *Proceedings of the SPIE*, edited by Ardeberg, A. L., and Andersen, T., Vol. 5382, 2004, pp. 337–345.

[5] Chanan, G., MacMartin, D. G., Nelson, J., and Mast, T., "Control and Alignment of Segmented-Mirror Telescopes: Matrices, Modes, and Error Propagation," *Applied Optics*, Vol. 43, No. 6, Feb. 2004, pp. 1223–1232. doi:10.1364/AO.43.001223

[6] Dimmler, M., Erm, T., Bauvir, B., Sedghi, B., Bonnet, H., Müller, M., and Wallander, A., "E-ELT Primary Mirror Control System," *Ground-Based and Airborne Telescopes II*, edited by L. Stepp, Vol. 7012, Society of Photo-Optical Instrumentation Engineers, Bellingham, WA, 2008, pp. 701210–701210-11.

[7] MacMynowski, D. G., Thompson, P. M., and Sirota, M. J., "Analysis of TMT Primary Mirror Control-Structure Interaction," *Modeling, Systems Engineering and Project Management for Astronomy III*, edited by G. Z. Angeli, and M. J. Cullum, Vol. 7017, Society of Photo-Optical Instrumentation Engineers, 2008, pp. 701715–701715-12.

[8] MacMynowski, D. G., Thompson, P. M., and Sirota, M. J., "Control of Many-Coupled Oscillators and Application to Segmented-Mirror Telescopes," *AIAA Guidance, Navigation and Control Conference*, AIAA Paper 2008-6638, Aug. 2008.

[9] Jiang, S., Voulgaris, P. G., Holloway, L. E., and Thompson, L. A., "$\mathcal{H}_2$ Control of Large Segmented Telescopes," *Journal of Vibration and Control*, Vol. 15, No. 6, 2009, pp. 923–949. doi:10.1177/1077546308091211

[10] Angeli, G. Z., Cho, M. K., and Whorton, M. S., "Active Optics and Architecture for a Giant Segmented Mirror Telescope," *Future Giant Telescopes*, edited by P. Angeli, and R. Gilmozzi, Society of Photo-Optical Instrumentation Engineers, Paper No. 4840-22, 2002, pp. 129–139.

[11] *The VLT White Book*, European Southern Observatory, Garching, Germany, 1998.

[12] Dimmler, M., E-ELT Programme: M1 Control Strategies, Rept. E-TRE-ESO-449-0211, No. 1, April 2008.

[13] Geradin, M., and Rixen, D., *Mechanical Vibrations*, 2nd ed., Wiley, New York, 1997, pp. 343.

[14] Craig, R. R., and Bampton, M. C. C., "Coupling of Substructures for Dynamic Analyses," *AIAA Journal*, Vol. 6, No. 7, 1968, pp. 1313–1319. doi:10.2514/3.4741

[15] Guyan, R. J., "Reduction of Stiffness and Mass Matrices," *AIAA Journal*, Vol. 3, No. 2, 1965, pp. 380. doi:10.2514/3.2874

[16] Aubrun, J. N., Lorell, K. R., Havas, T. W., and Henninger, W. C., "Performance Analysis of the Segment Alignment Control System for the Ten-Meter Telescope," *Automatica*, Vol. 24, No. 4, 1988, pp. 437–453. doi:10.1016/0005-1098(88)90090-8

[17] Aubrun, J. N., Lorell, K. R., Mast, T. S., and Nelson, J. E., "Dynamic Analysis of the Actively Controlled Segmented Mirror of the, W. M. Keck Ten-Meter Telescope," *IEEE Control Systems Magazine*, Vol. 7, No. 6, 3–10 Dec. 1987.

[18] Doyle, J. C., and Stein, G., "Multivariable Feedback Design: Concepts for a Classical/Modern Synthesis," *IEEE Transactions on Automatic Control*, Vol. AC-26, Feb. 1981, pp. 4–17.

[19] Maciejowski, *Multivariable Feedback Design*, Addison Wesley Longman, Reading, MA, 1989.

[20] Kosut, R. L., Salzwedel, H., and Emami-Naeini, A., "Robust Control of Flexible Spacecraft," *Journal of Guidance, Control, and Dynamics*, Vol. 6, No. 2, March–April 1983, pp. 104–111. doi:10.2514/3.56344

[21] Franklin, G. F., Powell, J. D., and Emani-Naemi, A., *Feedback Control of Dynamic Systems*, Addison Wesley Longman, Reading, MA, 1986, Chap. 6.

[22] Lurie, B. J., and Enright, P. J., *Classical Feedback Control*, Marcel Dekker, New York, 2000, Ch. 3.

[23] Preumont, A., Bastaits, R., and Rodrigues, G., "Active Optics of Large Segmented Mirrors: Scale Effects," *Invited Lecture, International Conference on Smart Structures and Materials*, Faculdade de Engenharia da Universidade do Porto, Porto, Portugal, July 2009, pp. 143–156.